Contributions to Mineralogy and Petrology (2021) 176:87
https://doi.org/10.1007/s00410-021-01849-7

ORIGINAL PAPER

Hydrothermal alteration processes of fluorapatite and implications for REE remobilization and mineralization

Bing Xiao[1,2] · Yuanming Pan[3] · Hao Song[4] · Wenlei Song[5] · Yu Zhang[6] · Huayong Chen[1,2]

Received: 29 April 2021 / Accepted: 28 September 2021 / Published online: 8 October 2021

Abstract

Apatite-rich rocks from marine phosphorites, alkaline igneous complexes, and iron-oxide copper gold (IOCG) deposits commonly contain elevated but sub-economic contents of rare earth elements (REE). In this study, we selected fluorapatite from the Paleoproterozoic Yinachang IOCG deposit in Southwest China to evaluate the mechanisms of REE remobilization, transportation and precipitation during fluorapatite alteration. Four texturally and compositionally distinct types of fluorapatite were identified. Ap1, related to mantle-derived magmatic-hydrothermal fluid from dolerite intrusions, contains the highest (REE + Y) content (> 1 wt%). Ap2 was directly deposited from a magmatic-hydrothermal fluid related to Cu mineralization, rich in Cl and S but poor in REE + Y. Pervasive REE-rich mineral inclusions and micro-pores in the altered domains from Ap1 and Ap3-1 indicate that extensive metasomatic alteration occurred via a coupled dissolution-reprecipitation process, which was related to a late oxidizing hydrothermal fluid. After the end of the dissolution-reprecipitation process, Ap3-2 formed through regrowth of Ap3-1. Ap4 in late monazite-sulfide veins has extremely high positive Eu anomalies (24–32) and the highest Eu contents, which are related to a late reduced hydrothermal fluid. This study demonstrates that the geochemical and textural features of altered fluorapatite from the Yinachang IOCG deposit were controlled by both a sorption processes and the oxidation states of the hydrothermal fluids. The most salient feature in the Yinachang deposit is that REE remobilization associated with the alteration of fluorapatite by Neoproterozoic hydrothermal fluids is not strictly localized in extent, and REE in fluorapatite can also be transported in distance and precipitate as REE-rich minerals in independent mineralized veins.

Keywords Fluorapatite · Metasomatic alteration · REE remobilization, REE transport and enrichment · IOCG deposit

Introduction

Rare earth elements (REE) are critical elements in a variety of modern high-tech applications due to their unique physical and chemical characteristics. The global demand for REE has increased significantly during recent decades (Haxel 2002; Hoshino et al. 2016). Fluorapatite is a common constituent occurring in iron-oxide copper gold (IOCG) deposits (Li et al. 2015; Krneta et al. 2017; Cherry et al. 2018), iron-oxide fluorapatite (IOA) deposits (Harlov et al. 2016; Zeng et al. 2016), and carbonatite-related REE deposits (Broom-Fendley et al. 2016; Chakhmouradian et al. 2017; Song et al. 2018; Hu et al. 2019; Ying et al. 2020). It generally accommodates substantial amounts of REE in its crystal lattice (from several thousands of ppm to several wt%; Hoshino et al. 2016), making it a potential target for economic REE mineralization.

Communicated by Daniela Rubatto.

✉ Huayong Chen
huayongchen@gig.ac.cn

1 Key Laboratory of Mineralogy and Metallogeny, Guangzhou Institute of Geochemistry, Chinese Academy of Sciences, Guangzhou 510640, China

2 CAS Center for Excellence in Deep Earth Science, Guangzhou 510640, China

3 Department of Geological Sciences, University of Saskatchewan, Saskatoon, SK S7N 5E2, Canada

4 Chengdu University of Technology, Chengdu 610059, Sichuan, China

5 State Key Laboratory of Continental Dynamics, Department of Geology, Northwest University, Xi'an 710069, China

6 School of Geosciences and Info-Physics, Central South University, Changsha 410083, China

In addition, fluorapatite is capable of incorporating a wide variety of trace elements (Pan and Fleet 2002; Hughes and Rakovan 2015; Engi 2017), making it a good indicator of fluid evolution and mineralization processes (Harlov 2015; Andersson et al. 2019). Moreover, fluorapatite often contains elevated U and Th contents, and is widely used in U–Pb thermochronometry (Chew and Spikings 2015). Previous investigations have shown that REE can be released to form REE-rich inclusions when fluorapatite interacts with fluids during late hydrothermal alteration in IOCG, IOA and carbonatite-related REE deposits, which served as one of the dominant sources of REE mineralization (Li and Zhou 2015; Harlov et al. 2016; Broom-Fendley et al. 2016; Zeng et al. 2016; Krneta et al. 2017; Hu et al. 2019; Cherry et al. 2018; Ying et al. 2020). Nevertheless, our understanding of the mechanisms behind REE transportation and enrichment during hydrothermal metasomatism is still inadequate (Harlov et al. 2005; Bonyadi et al. 2011).

The Yinachang Fe–Cu–REE deposit, one of the important Fe–Cu–REE deposits in Southwest China (Fig. 1a), contains approximately 20 Mt ore at 41.9–44.5 wt % Fe and 15 Mt ore at 0.85–0.97 wt % Cu, with abundant REE (Zhao et al. 2015). Li et al. (2015) and Zhao et al. (2015) have shown that features of the Yinachang deposit are similar to those of IOCG deposits, and its REE mineralization is related to fluid-induced metasomatic alteration of REE-rich fluorapatite by late stage hydrothermal fluids associated with Cu mineralization. Due to the lack of suitable materials for high quality dating and a limited previous study on the internal structures of fluorapatite, timing the alteration of the fluorapatite as well as REE transport and enrichment mechanism of REE during fluorapatite alteration in the Yinachang deposit remain unclear.

In this study, we present a detailed documentation of fluorapatite textures from different stages of the Yinachang deposit using combined cathodoluminescence (CL), backscattered electron (BSE), and TESCAN integrated mineral analyzer (TIMA) imaging. Integrating these textural relationships with electron microprobe analysis (EMPA), laser ablation inductively coupled plasma mass spectrometry (LA–ICP–MS), micro-Raman spectroscopy, and U–Pb dating, we aim to evaluate the processes behind REE transport and enrichment during fluorapatite alteration and constrain the timing of REE mineralization in the Yinachang deposit.

Deposit geology and petrography

The Yinachang deposit is situated in the central part of the Kangdian metallogenic province, southwest of the Yangtze Block (Fig. 1a; Zhao et al. 2013; Zhou et al. 2014). The main lithostratigraphic units in the deposit area are the Proterozoic Yinmin, Luoxue, and E'touchang formations, and Mesozoic strata (Fig. 1b). Ore bodies, controlled by NNE-trending faults, are hosted in slate, schist, and dolostone of the Yinmin Formation, which was intruded by Paleoproterozoic dolerite intrusions (zircon $^{207}Pb/^{206}Pb$ U–Pb age of 1690 ± 32 Ma, Zhao et al. 2010). The detailed geology and metallogeny of the Yinachang deposit have been reviewed by Zhao et al. (2013) and Li and Zhou et al. (2015).

Combined with the study of Li and Zhou (2015) and Li et al. (2015), we divided hydrothermal alteration and

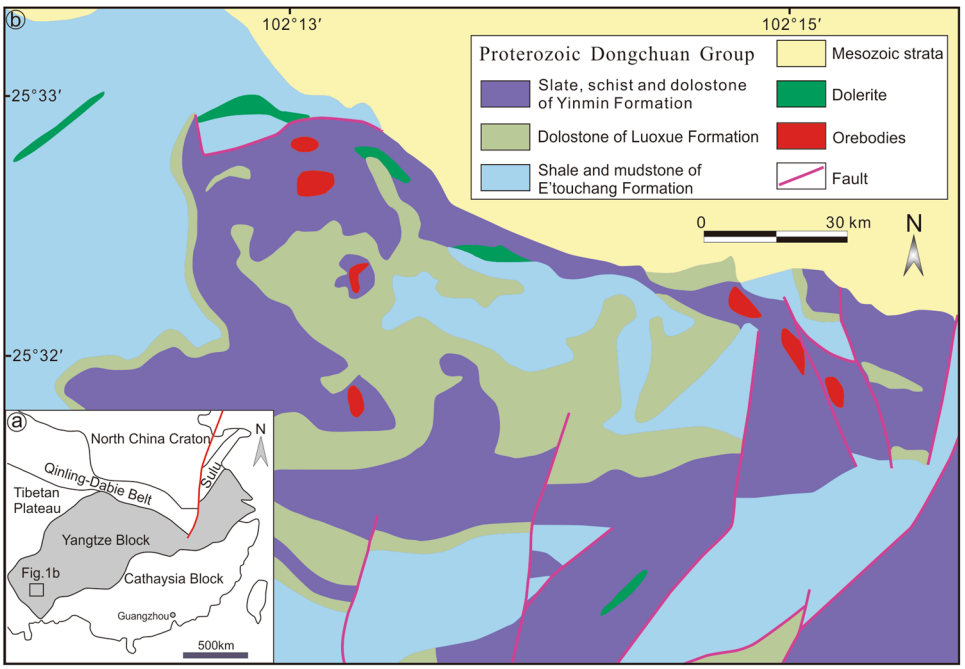

Fig. 1 **a** Simplified tectonic map of South China. **b** Geological map of the Yinachang deposit (modified from Li et al. 2015)

mineralization at the Yinachang deposit into three stages, including pre-ore Na–Fe alteration, Fe–Cu (–REE) mineralization and REE (–Cu) remobilization (Fig. 2). The Fe–Cu (–REE) mineralization stage contains early Fe (–REE) and late Cu (–REE) mineralization sub-stages (Li et al. 2015). The earliest Na–Fe alteration minerals in ore-hosting rocks are albite, quartz, magnetite, and hematite. The Fe (–REE) mineralization is characterized by the formation of magnetite, siderite, quartz, REE-rich fluorapatite, and less amounts of fluorite and ankerite (Figs. 3a and 4a). The subsequent Cu (–REE) mineralization is featured by abundant sulfide minerals (mainly chalcopyrite) and quartz, accompanied with subordinate biotite, calcite, fluorapatite (Figs. 3b, c and 4b), and REE-rich minerals [e.g., allanite, monazite–(Ce), bastnaesite-(Ce) and synchysite–(Ce); Li et al. 2015]. The REE (–Cu) remobilization stage, which is characterized by the formation of REE-rich minerals [e.g., monazite–(Ce) and synchysite–(Ce)], can be subdivided into two sub-stages (Fig. 2). The early REE (–Cu) remobilization is recorded by metasomatic alteration of REE-rich fluorapatite with abundant mineral inclusions [monazite–(Ce), quartz, hematite, bastnaesite–(Ce)] occurring in the alteration domains (Figs. 3d, e and 4c). The late REE (–Cu) remobilization is characterized by hydrothermal veins containing chalcopyrite, molybdenite, arsenopyrite, fluorapatite, monazite–(Ce), synchysite–(Ce) and magnetite (Figs. 3f and 4d). In this remobilization stage, the late chalcopyrite clearly replaced and cut the early altered REE-rich fluorapatite (Fig. 3e).

Sampling and analytical procedures

In this study, a total of 20 samples, 10 from the ore bodies and 10 from the country rocks (mainly schist and dolostone) were collected. Polished thin sections of these samples were first examined using transmitted and reflected light microscopy, and then BSE and CL imaging to characterize textural relationships and establish different stages of metasomatic alteration, i.e., Fe-REE mineralization stage (Ap1), Cu mineralization stage (Ap2), early REE (–Cu) remobilization stage (Ap3), and late REE (–Cu) remobilization stage (Ap4). Representative samples were then analyzed by in-situ Raman, TIMA, EMPA, and LA–ICP–MS to determine compositional and structural characteristics. EPMA, LA–ICP–MS and U–Pb dating results are listed in Electronic Supplementary Material 1.

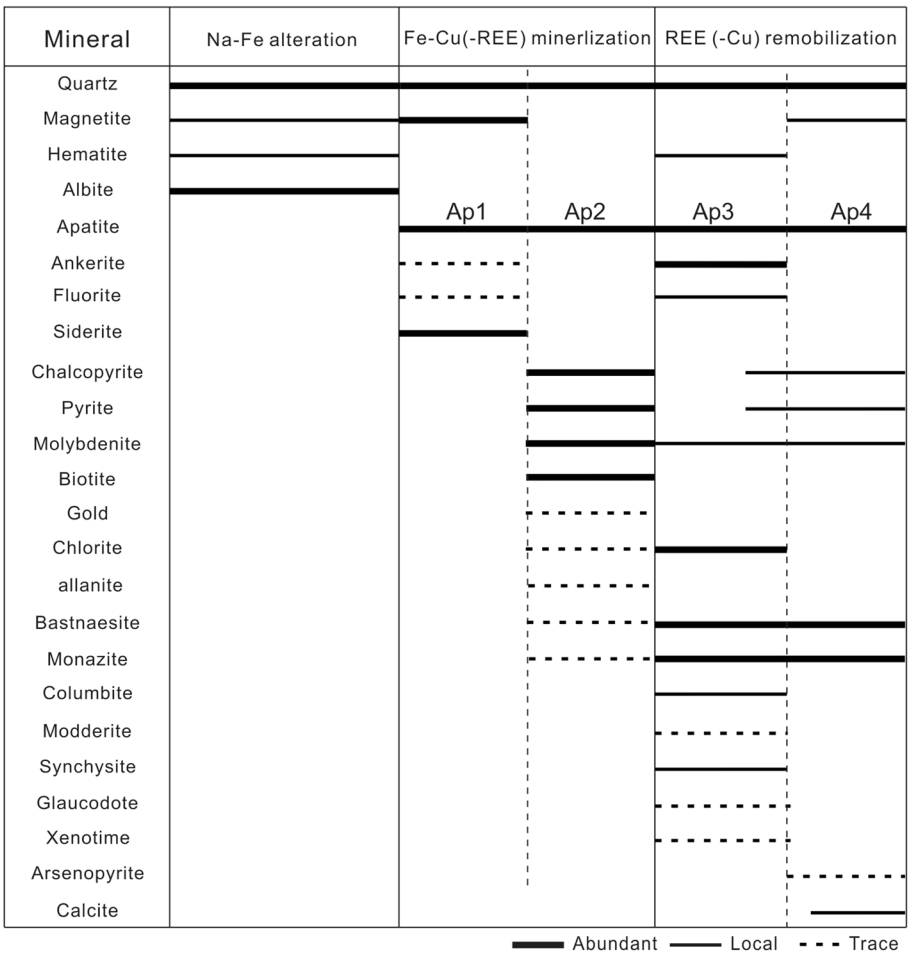

Fig. 2 Alteration and mineralization paragenesis of the Yinachang deposit, modified from Li et al. (2015) and Li and Zhou (2015)

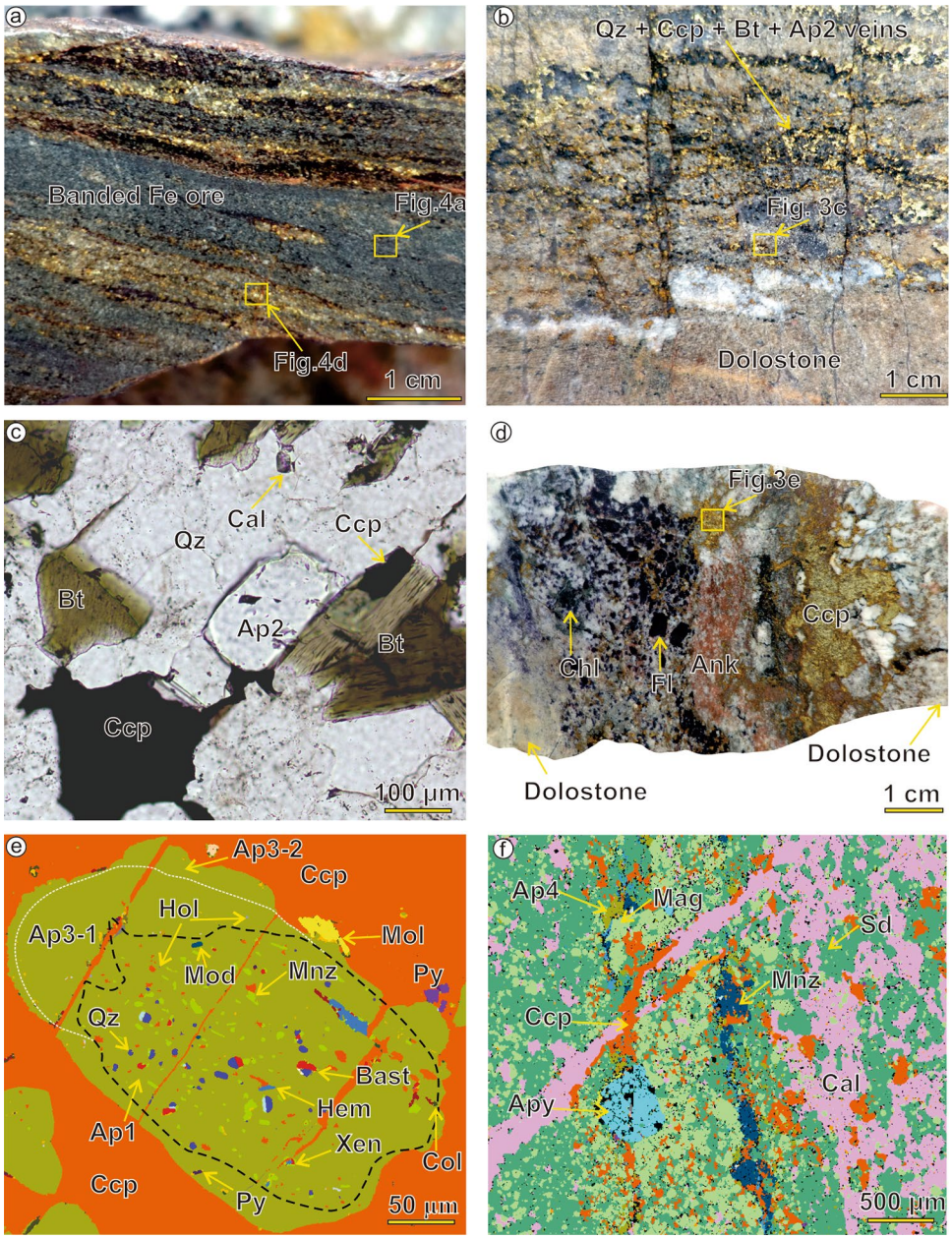

Fig. 3 Representative hand specimen photographs and microphotographs showing representative mineral assemblages, textural features of the Yinachang deposit. **a** Banded Fe ore, which contains sub-parallel, chalcopyrite-rich bands. **b** Quartz + chalcopyrite + biotite + fluorapatite veins intersect dolostone. **c** Fluorapatite grains (Ap2) in Cu ore, coeval with quartz, chalcopyrite, and biotite. **d** A wide quartz + chalcopyrite + ankerite + fluorapatite + fluorite + molybdenite + chlorite + pyrite vein intersecting dolostone. **e** TIMA image showing the mineral inclusions and micro-pores in altered domains of the original Ap1. **f** TIMA image showing a chalcopyrite + magnetite + fluorapatite (Ap4) + synchysite-(Ce) + monazite-(Ce) + molybdenite vein intersecting a banded Fe ore. Mineral abbreviations: *Ank* ankerite, *Ap* fluorapatite, *Apy* arsenopyrite, *Bast* bastnaesite–(Ce), *Bt* biotite, *Ccp* chalcopyrite, *Cal* calcite, *Chl* chlorite, *Col* columbite, *Fl* fluorite, *Hol* hole, *Hem* hematite, *Mag* magnetite, *Mnz* monazite–(Ce), *Mod* modderite, *Mol* molybdenite, *Py* pyrite, *Qz* quartz, *Sd* siderite, *Syn* synchysite–(Ce), *Xen* xenotime

BSE and CL imaging was carried out on polished thin sections using a TESCAN MIRA3 field-emission scanning electron microprobe (FE-SEM) at the Testing Center, Tuoyan Analytical Technology Co. Ltd., Guangzhou, China. After the samples were carbon-coated, SEM-CL images were acquired under an acceleration voltage of 10 kV and a beam current of 15 nA. Mineral compositional mapping was obtained on carbon-coated thin sections using a MIRA3 scanning electron microscope equipped with two energy dispersive X-ray spectrometers (EDS, EDAX Element) (TIMA) at the State Key Laboratory of Continental Dynamics, Department of Geology, Northwest University, Xian, China. An acceleration voltage of 25 kV and a beam current of 9 nA were used. The current and BSE signal intensity were calibrated on a platinum Faraday cup using the automated procedure. The EDS intensities were then normalized using a Mn standard. The samples were also scanned using a TIMA liberation analysis module.

Major and minor element analyses of selected fluorapatite grains were conducted using a Cameca SX100 electron microprobe at the Guangzhou Institute of Geochemistry, Chinese Academy of Sciences (GIGCAS), Guangzhou, China. The following conditions were used for measurements of all standards and samples: 15 kV accelerating voltage, 20 nA beam current, 1 μm beam diameter, and 10 s counting time. To correct for the matrix effects during

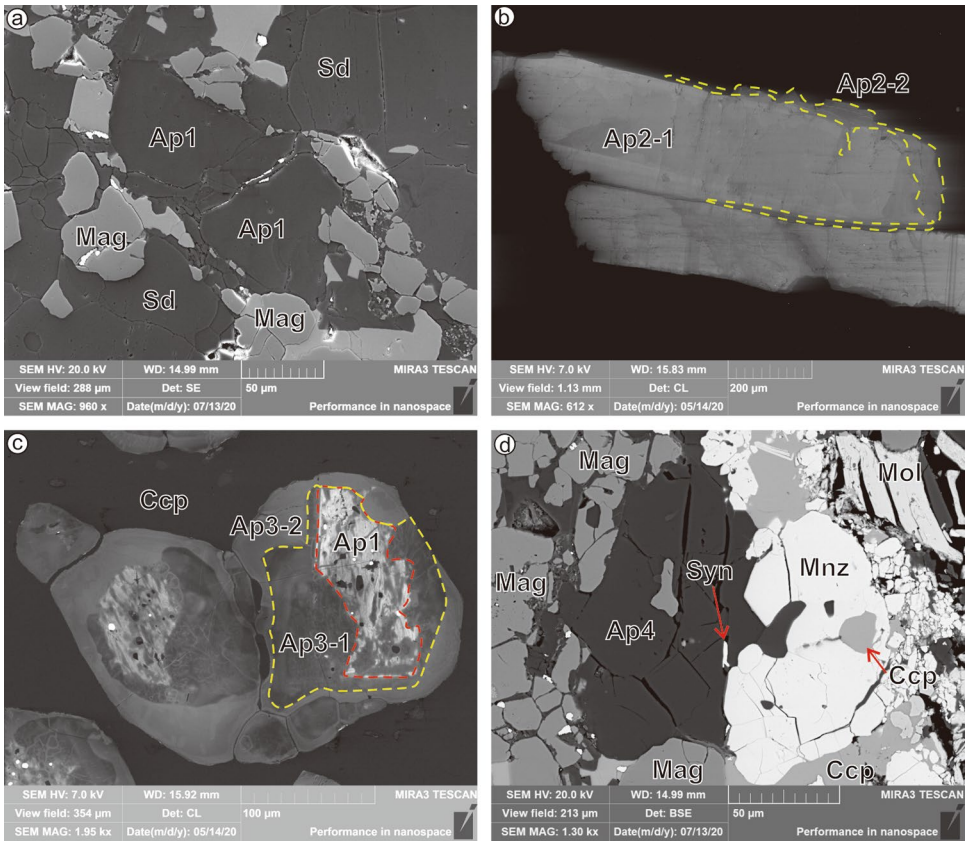

Fig. 4 Representative BSE and CL images showing textural features of fluorapatite in the Yinachang deposit. **a** BSE image of unaltered REE-rich fluorapatite grains (Ap1) in banded Fe ore, intimately associated with coeval siderite and magnetite. **b** CL image of fluorapatite in Cu ore showing a bright and irregular core (Ap2-1) and a dark mantle (Ap2-2). **c** CL image showing Ap3-1 formed during fluid-induced metasomatic alteration of Ap1. Ap3-2 occurs as an overgrowth margin around Ap3-1. Note that pervasive REE-rich mineral inclusions or micro-pores are present in altered domains from the original Ap1. **d** BSE image of a chalcopyrite + magnetite + fluorapatite (Ap4) + synchysite-(Ce) + monazite-(Ce) + molybdenite vein intersecting a banded Fe ore. Mineral abbreviations: *Ap* fluorapatite, *Ccp* chalcopyrite, *Mag* magnetite, *Mnz* monazite–(Ce), *Mol* molybdenite, *Sd* siderite, *Syn* synchysite–(Ce)

EPMA, the ZAF correction was applied to transform the relative peak intensities into the elemental weight composition (Bernard et al. 1986). The relative precisions of EPMA are < 2% for major elements and < 5% for minor elements.

In situ U–Pb and trace element analyses of fluorapatite were made using a NWR laser ablation system coupled with an inductively coupled plasma mass spectroscopy (ICP-MS, model: iCAP RQ) at the Tuoyan Analytical Technology Co. Ltd., Guangzhou, China. The details of LA-ICP-MS analyses have been given as tables in Electronic Supplementary Material 2. Analyses were calibrated using two external standards (SRM-610 and SRM-612) for trace elements analysis, and Madagascar (MAD) and Durango (DUR) apatite as internal and external standards for U–Pb dating, respectively. Repeated analyses yielded $^{206}Pb/^{238}U$ ages of 474.5 ± 4.5 Ma for MAD and 30.9 ± 0.6 Ma for DUR, which were in good agreement with the recommended MAD $^{206}Pb/^{238}U$ age of 474.3 ± 0.4 Ma (Thomson et al. 2012) and DUR $^{206}Pb/^{238}U$ age of 31.13 ± 1.01 Ma (McDowell et al. 2005), respectively.

Raman spectra from fluorapatite were collected using a RM2000 laser micro-Raman spectrometer at GIGCAS. A 514.5 nm Ar laser was used, with a 2 µm diameter laser spot is 2 µm in diameter. The scanning range was between 100 and 1500 cm^{-1} with a spectral resolution of 1 cm^{-1}. The laser power reaching the sample surface was 10 mW and the typical acquisition time was 60 s to avoid laser-induced thermal effects and oxidation.

Results

Textural and structural characteristics of fluorapatite

Ap1, commonly developed in Fe ores (Fig. 3a), is typically euhedral to subhedral in shape with variable sizes of 20–200 µm in the maximum dimension. The unaltered Ap1 grains are relatively homogeneous under CL imaging (Fig. 4a). Ap2 with few REE mineral inclusions, coexisting with chalcopyrite, biotite, calcite, and quartz (Fig. 3c), exhibits elongated morphology with variable lengths of 100–1500 µm, and contains a bright and irregular core (Ap2-1) with a dark mantle (Ap2-2) in the CL image (Fig. 4b). Ap3 occurs in close association with chalcopyrite and often as a replacement after Ap1 (Fig. 4c). It can be subdivided into Ap3-1 and Ap3-2 on the basis of CL imaging. Abundant mineral inclusions [hematite, pyrite, modderite ((Co, Fe)As), monazite-(Ce), quartz, synchysite-(Ce) ($CaCe(CO_3)_2F$), bastnaesite-(Ce) ($CeCO_3F$)] and micro-pores are developed in the reaction front (i.e., dark domains in Ap1, Fig. 4c) between Ap1 and Ap3-1 (Figs. 3e and 4c), while lesser but

larger inclusions and micro-pores are developed when Ap1 was completely replaced by Ap3-1. Compared with Ap1, Ap3-1 is darker under BSE and CL imaging. Ap3-2 with brighter CL occurs as an overgrowth around Ap3-1. Ap4 is coeval with chalcopyrite, molybdenite, synchysite-(Ce), monazite-(Ce), and magnetite in the hydrothermal veins (Fig. 3f), and has homogeneous CL (Fig. 4d).

All fluorapatite grains at Yinachang exhibit Raman bands characteristic of fluorapatite, including a strong peak at ~ 965 cm^{-1} and a weak peak at 582–616 cm^{-1} (Fig. 5; Chakhmouradian et al. 2017). In addition, Ap1 and Ap3-2 have the more obvious Si–O vibration modes at 395 and 811–838 cm^{-1}, and the S–O vibration modes at 640 and 1114–1186 cm^{-1} than other fluorapatite at Yinachang. The carbonate ν_4 vibration mode at ~ 700 cm^{-1} (Awonusi et al. 2007) is also visible in Ap1 and Ap3-2 (Fig. 5).

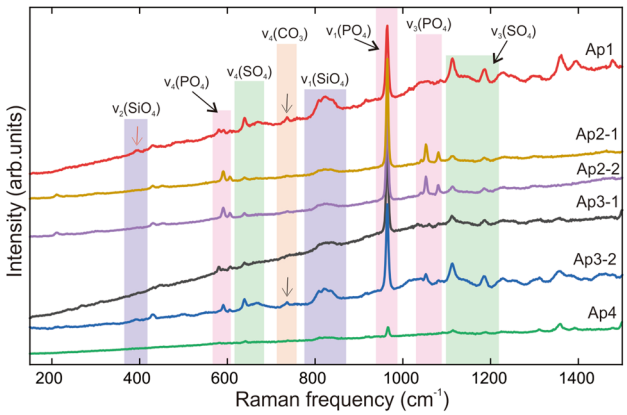

Fig. 5 Raman spectra measured in situ on the four kinds of fluorapatite from the Yinachang deposit. Characteristic vibration modes of carbonate, phosphate, silicate and sulfate groups are marked. Note that Ap1 and Ap3-2 have the more obvious Si–O, S–O and C–O vibration modes than Ap2-1, Ap2-2, Ap3-1 and Ap4

Chemical composition of fluorapatite

Of the four fluorapatite types, Ap1 contains the highest SiO_2 content, Ap2 has the highest Cl content, Ap4 contains the highest FeO content, and Ap2-1 has the lowest MnO content (Fig. 6). Compared with Ap2, Ap3, and Ap4, Ap1 contain the highest REE + Y content (> 1 wt%; Electronic Supplementary Material 1). Ap4 is characterized by LREE-enriched, chondrite-normalized REE patterns with slightly negative to moderately positive Eu anomalies (Fig. 7a; 0.78–4.03; Electronic Supplementary Material 1). The degree of LREE enrichment relative to HREE for Ap1, represented by the $(La/Yb)_N$ ratio, varies between 6.20 and 67 (Electronic Supplementary Material 1). Ap2-1, Ap2-2, Ap3-1, and Ap3-2 all display MREE-enriched chondrite-normalized REE patterns (Figs. 7b and c) with similar positive Eu anomalies (1.66–3.32; Electronic Supplementary Material 1). Ap4, similar to Ap1, shows LREE-enriched chondrite-normalized REE patterns with the $(La/Yb)_N$ ratio ranging from 24 to 52 (Electronic Supplementary Material 1), the most pronounced positive Eu anomalies (24–32; Electronic Supplementary Material 1), and the highest Eu contents (Fig. 7d). These positive Eu anomalies in Ap4 represent some of the highest values known for apatite-group minerals (Fleet and Pan 1995; Krneta et al. 2017; Algabri et al. 2020; Bromiley 2021).

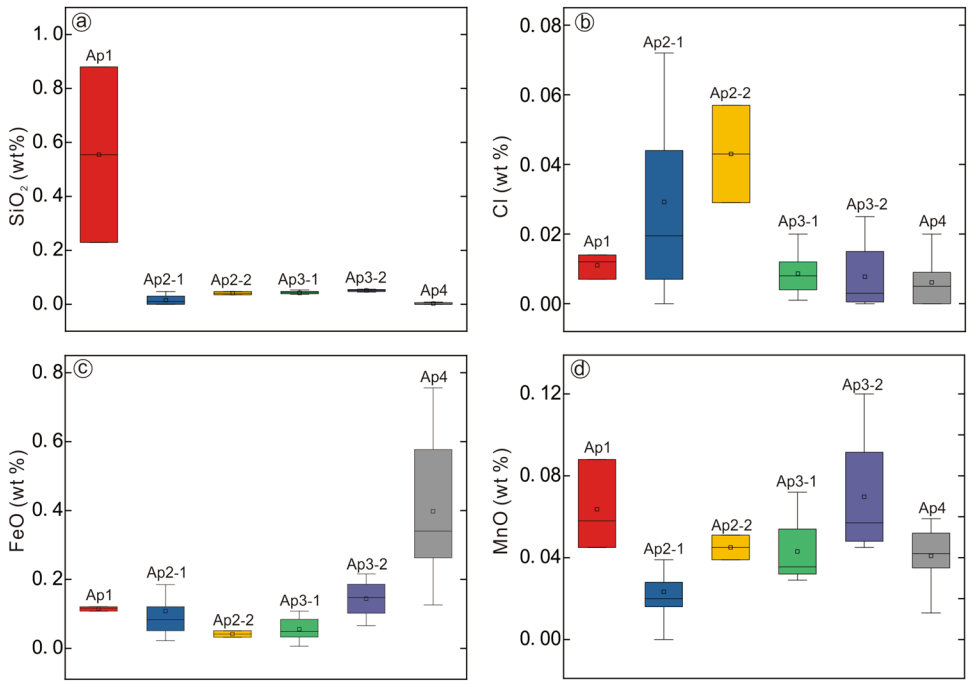

Fig. 6 The ranges in the SiO_2 **a**, Cl **b**, FeO **c**, and MnO **d** contents in fluorapatite fromthe Yinachang deposit. Note that Ap1 contains the highest SiO_2 content, Ap2 has the highest Cl content, Ap4 contains the highest FeO content, and Ap2-1 has the lowest MnO content. The data of Ap1 are obtained from Li and Zhou (2015)

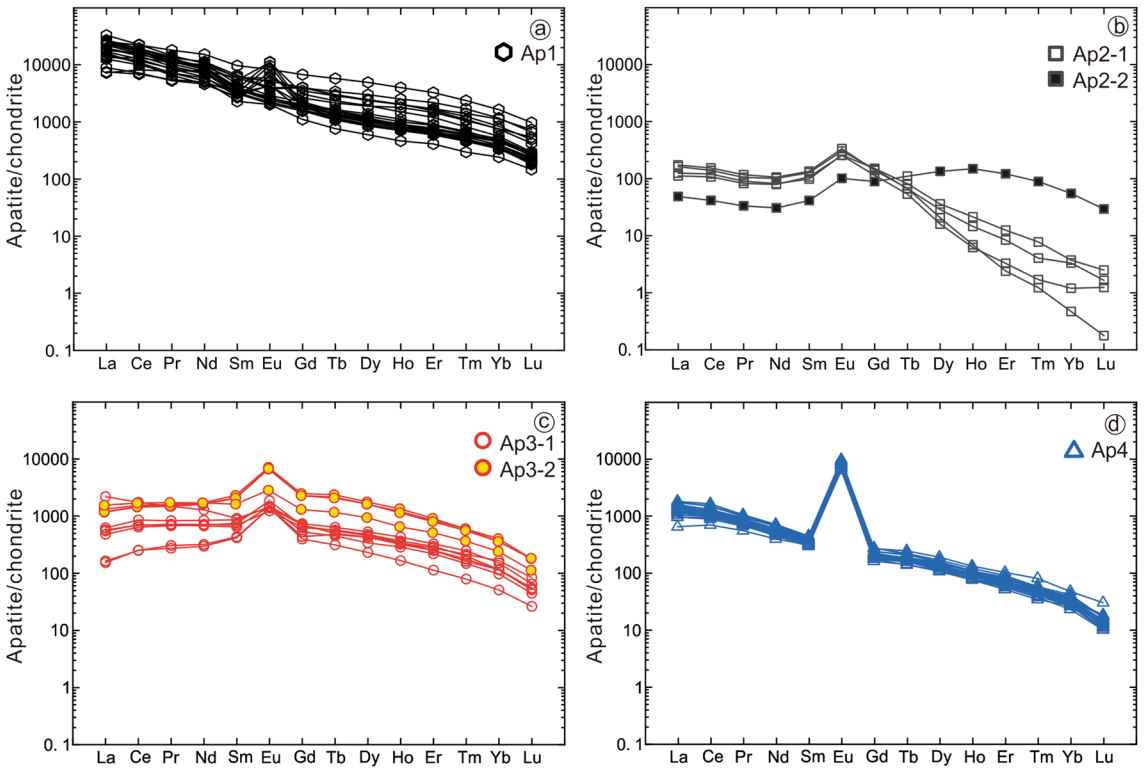

Fig. 7 Chondrite-normalized REE patterns for the four stages of fluorapatite from theYinachang deposit. Note that Ap1 contain the highest REE + Y content than Ap2, Ap3, and Ap4. The data of Ap1 are obtained from Li and Zhou (2015)

U–Pb geochronology of fluorapatite

Due to the low U contents of Ap2 and the high common Pb contents of Ap1 and Ap4, only Ap3 was suitable for U–Pb dating. A total of 29 laser ablation spots from 10 Ap3-1 grains were obtained for U–Pb geochronology, which defined a regression line on the Tera-Wasserburg plot, with a lower intercept age of 939.6 ± 17.6 Ma (MSWD = 0.89, $n = 27$; Fig. 8). We consider the lower intercept age to indicate the timing of Ap3-1 formation.

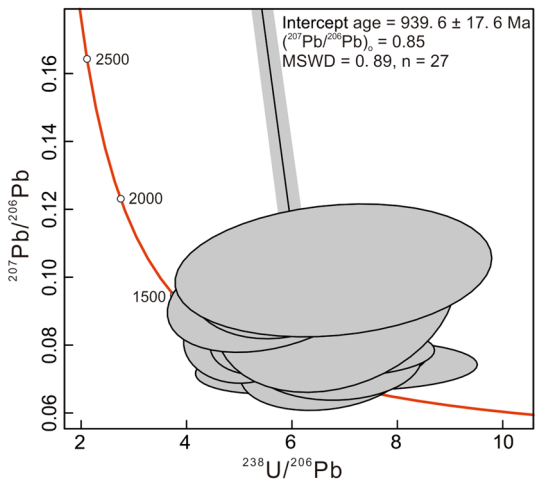

Fig. 8 LA–ICP–MS U–Pb Tera–Wasserburg concordia diagram for Ap3-1

Discussion

Metasomatic alteration of fluorapatite and substitution mechanisms

In this contribution, combined BSE-CL images and TIMA data as well as Raman spectra highlight the complicated textures for the different stages of fluorapatite in the Yinachang deposit, which were not fully revealed by previous SEM imaging (Li and Zhou 2015; Zhao et al. 2015). TIMA studies show that pervasive REE-rich mineral inclusions and micro-pores are present in altered domains in the original Ap1 (Fig. 3e), which have long been documented by both natural and experimental studies (Pan et al. 1993; Harlov and Förster 2003; Li and Zhou 2015; Harlov et al. 2016; Krneta et al. 2017). In addition, a close spatial relationship and obvious reaction fronts were observed between Ap1 and Ap3-1 (Fig. 4c), indicating that extensive metasomatic alteration occurred by means of a

coupled dissolution (Ap1)-reprecipitation (Ap3-1) process (Pan et al. 1993; Harlov et al. 2005; Putnis 2009). Different Raman signatures of Ap1 and Ap3-1 imply that structural and chemical changes occurred along with the leaching of REE from the fluorapatite (Fig. 5). Compared with Ap1, Ap3-1 has a lower Si and REE + Y content, indicating that Si in Ap1 was removed by a hydrothermal fluid resulting in charge imbalance, which promoted the dissolution-reprecipitation process and freed the (REE + Y) to react with PO_4^{3-} and CO_3^{2-} groups to form monazite–(Ce) and bastnaesite–(Ce) micro-inclusions. In addition, CL images show that Ap3-2 and Ap2-2 occur as an overgrowth around Ap3-1 and Ap2-1, respectively, without mineral inclusions or micro-pores between them.

The REE + Y contents of Ap1 have a positive correlation with Si but invariably lie slightly above the 1:1 molar ratio line (Fig. 9a). This result suggests that the coupled substitution, $Si^{4+} + (REE + Y)^{3+} = P^{5+} + Ca^{2+}$ (Fleet and Pan 1995; Pan and Fleet 2002), is dominant. However, other substitution mechanisms such as $C^{4+} + (REE + Y)^{3+} = P^{5+} + Ca^{2+}$ may have contributed as well, which is supported by the elevated carbonate revealed by the Raman spectrum of Ap1 (Fig. 5). However, the REE + Y values in Ap2-1, Ap2-2, Ap3-1, Ap3-2, and Ap4 are strongly positively correlated with Na (Fig. 9b), while only show a weakly positive correlation with Si, suggesting that the coupled substitution, $Na^{+} + (REE + Y)^{3+} = 2Ca^{2+}$ (Fleet and Pan 1995; Pan and Fleet 2002) predominates. These results suggest that the REE substitution mechanisms in fluorapatite changed with time in the Yinachang deposit.

Timing of REE remobilization and fluorapatite alteration

Li and Zhou (2015) suggested that the Sm–Nd isochron age of 1700 Ma represents the timing of Fe (–REE) mineralization (hosting Ap1), consistent with the formation age of the dolerite intrusions (zircon U–Pb age of 1690 ± 32 Ma; Zhao et al. 2010), indicating a direct genetic relationship between Fe (-REE) mineralization and the dolerite intrusions. Re-Os dating of molybdenite and chalcopyrite yields ages of 1660–1690 Ma for the main Cu (–REE) mineralization (hosting Ap2) at Yinachang (Ye et al. 2013; Zhao et al. 2013), which resulted in alteration of REE-rich fluorapatite (Ap1) and REE mineralization (Li et al. 2015; Li and Zhou 2015). In this study, in situ U–Pb analysis of Ap3 demonstrates that the REE (–Cu) remobilization stage of the Yinachang deposit occurred at ~ 940 Ma, which is obviously younger than the age of the major Fe-Cu (-REE) mineralization event. In addition, Li and Zhou (2015) also reported that monazite-(Ce) grains associated with Ap4 have a U–Pb age of 842 ± 9 Ma. Aside from the REE-rich Ap1 alteration event at the Fe–Cu (–REE) mineralization stage (1700 Ma, Li and Zhou 2015), these absolute ages indicate that intensive alteration of REE-rich apatite and remobilization of REE and Cu in the Yinachang deposit also occurred at 940–840 Ma, which is consistent with recently identified Cu mineralization events at 1000–800 Ma in this region (Zhao et al. 2017). In fact, magmatic events of 1000–800 Ma in the Kangdian metallogenic province have been widely documented over the last two decades (Zhou et al. 2002, 2014; Li et al. 2006; Zhao et al. 2017; Su et al. 2021).

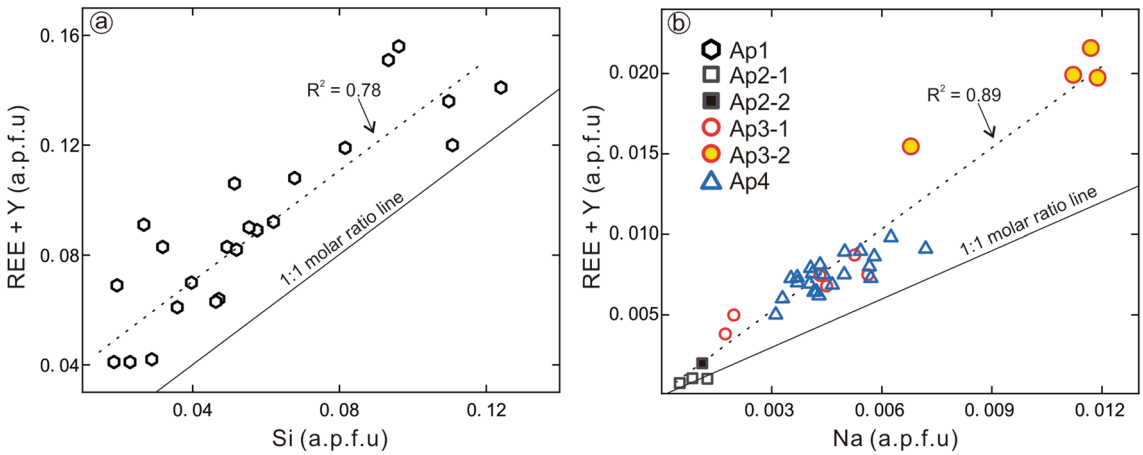

Fig. 9 Binary diagrams showing the substitution mechanisms of REE in Yinachang fluorapatite **a** REE + Y vs. Si; **b** REE + Y vs. Na. Note that the 1:1 solid lines in **a**, which indicate the coupled substitution $Si^{4+} + (REE + Y)^{3+} = P^{5+} + Ca^{2+}$ and the solid lines in **b**, which indicate the substitution $Na^{+} + (REE + Y)^{3+} = 2Ca^{2+}$. The data of Ap1 are obtained from Li and Zhou (2015)

Physical–chemical controls on REE mobility during fluorapatite alteration

The previously reported Sm–Nd isochron age (1700 Ma) from the Yinachang Fe ore samples (Li and Zhou 2015) is consistent with the Paleoproterozoic age of the mantle-derived dolerite intrusions in the ore district. Interestingly, Ap1 and the dolerite intrusions have similar initial $^{87}Sr/^{86}Sr$ ratios (0.704–0.710 and 0.706–0.707; Zhao et al. 2015). Fluid temperatures for Fe (–REE) mineralization estimated from oxygen isotope thermometry on the magnetite-siderite pair range from 395 to 503 °C (Li et al. 2015). Hence, Ap1 coeval with magnetite was most likely related to a high temperature magmatic-hydrothermal fluid, which was rich in REE + Y and CO_2, as seen by the presence of co-existing REE-rich Ap1 and siderite ($FeCO_3$) (Fig. 4a) as well as the presence of carbonate in the Raman spectrum of Ap1 (Fig. 5). $\delta^{34}S$ values of the ore-forming fluids in the Cu (–REE) mineralization sub-stage and the REE (–Cu) remobilization stage have a concentrated range near 0‰ (− 2.8 to + 2.7‰; Li et al. 2015), just overlapping the compositional fields of magmatic derived S (~ 0‰; Ohmoto and Rye 1979), suggesting that Ap2, Ap3, and Ap4 are also related to a magmatic-hydrothermal fluid.

Europium L_3-edge X-ray absorption near edge structure (XANES) spectroscopic analyses of natural and synthetic fluorapatite have shown that Eu exists in both the divalent and trivalent states (Rakovan et al. 2001). Previous studies indicate that fluorapatite usually displays negative or no Eu anomalies (Fleet and Pan 1995; Mao et al. 2016; Bromiley 2021), although positive Eu anomalies in fluorapatite have been reported in the literature, such as the Olympic Dam IOCG deposit (Krneta et al. 2017). In this study, the Yinachang Ap1 displays slightly negative to moderate positive Eu anomalies, whereas, Ap2, Ap3, and Ap4 all show obviously positive Eu anomalies (Fig. 7). Hence, the positive Eu anomalies of Ap2, Ap3, and Ap4 were not inherited from Ap1, but record the effects of the hydrothermal fluids during the Cu–Au–REE mineralization stage. Hydrothermal fluids with positive Eu anomalies have been reported to occur in the following two scenarios. First, magmatic feldspars, especially plagioclase, usually show strongly positive Eu anomalies due to the preferential incorporation of Eu^{2+}, which could be transferred into the hydrothermal fluid through their dissolution. This process has been proposed to be responsible for seafloor hydrothermal fluids with remarkably uniform chondrite-normalized REE patterns characterized by LREE enrichment and large positive Eu anomalies (Klinkhammer et al. 1994; Hoshino et al. 2016). Second, previous studies also have shown that if the REE pattern of hydrothermal fluids is controlled by sorption processes, the decreasing ionic radius of the trivalent REE leads to $(La/Lu)_{cn} > 1$, and the larger ionic radius of the Eu^{2+} ion compared to that of neighboring Sm^{3+} and Gd^{3+} causes positive Eu anomalies. But if the pattern is controlled by complex mechanisms, this decrease in radius will result in $(La/Lu)_{cn} < 1$. Note that sericite or other K-rich minerals are conspicuously absent during the Cu (–REE) mineralization and REE (–Cu) remobilization stage and the $(La/Lu)_{cn}$ values of Ap2, Ap3, and Ap4 are all above 1. Therefore, the positive Eu anomalies in Ap2, Ap3, and Ap4 could not be related to feldspar dissolution, but may be accounted for by the sorption processes and the reduction of Eu^{3+} to Eu^{2+} (Bau 1991).

The study of Li and Zhou (2015) identified two types of fluorapatite formed through dissolution-reprecipitation processes during REE-rich fluorapatite (Ap1) alteration: Type I fluorapatite with few REE mineral inclusions formed at the Cu (–REE) mineralization stage, and Type II fluorapatite hosting abundant REE mineral inclusions formed at the REE (–Cu) remobilization stage corresponding to Ap3 in this study. Hand specimen photographs and microphotographs show that Ap2 intergrows with chalcopyrite in the hydrothermal veins (Fig. 3b and c), indicating that Ap2 was directly deposited from the aforementioned magmatic-hydrothermal fluid related to Cu mineralization. Compared with Type I fluorapatite (480–6300 ppm) in the study of Li and Zhou (2015), the total REE contents of Ap2 (~ 200 ppm; Electronic Supplementary Material 1) are obviously lower, indicating that Ap2 formed from the hydrothermal fluid before leaching REE from REE-rich Ap1. The total REE contents of Ap2 are the lowest among all kinds of fluorapatite in the Yinachang deposit (Fig. 7), indicating that the original Cu (–REE) mineralization stage fluids was REE-poor. Ap3-1 formed through the reprecipitation with dissolution of REE-rich Ap1 during metasomatic replacement. Previous studies have shown that hydrothermal fluids leaching REE from fluorapatite typically have low Na and/or Si, because these elements in the fluids can enter the fluorapatite lattices to maintain an electrovalent balance, thereby inhibiting the removal of REE from fluorapatite (Harlov et al. 2003). In addition, the coeval relationships of hematite, ankerite, and fluorite with Ap3-1 indicate a relatively high oxidation state for the magmatic-hydrothermal fluids, which are rich in sulfate, F, Ca, and CO_2, and depleted in REE + Y. The relatively high oxidation state of the magmatic-hydrothermal fluids during the formation Ap3-1 is also supported by the detection of the sulfate group in their Raman spectra (Fig. 5). Compared with Ap3-1, Ap3-2 with clean homogenous CL image has higher total REE content (Fig. 7c), indicating Ap3-2 may have formed through regrowth of Ap3-1, after the end of the dissolution-reprecipitation process, which resulted in increasing REE content of hydrothermal fluid through leaching REE from REE-rich Ap1. The occurring of F-rich REE minerals [synchysite-(Ce), bastnaesite-(Ce) and fluorite] in the REE (–Cu) remobilization stage

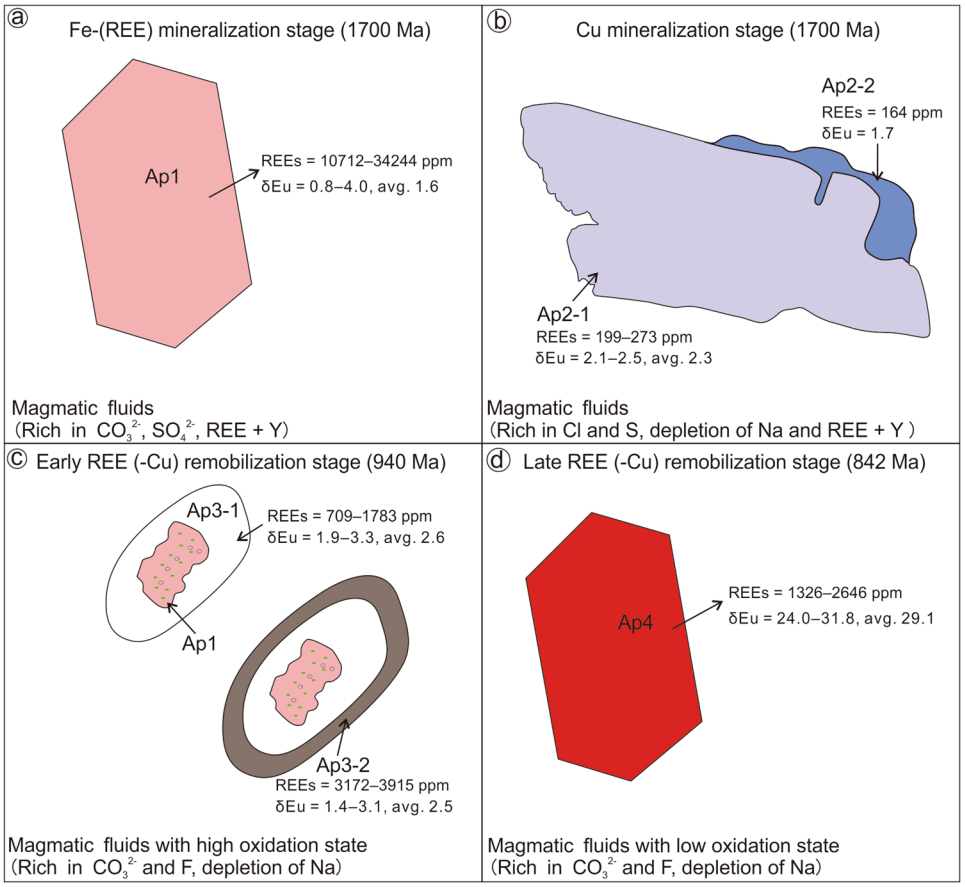

Fig. 10 Sketches illustrating the various stages in the formation of Ap1, Ap2, Ap3, and Ap4 in the Yinachang deposit

provides support for the F-rich composition of the hydrothermal fluid, which might explain the common occurrence of micro-pores in Ap1 due to F-induced dissolution (Zhou et al. 2009).

Compared with Ap2 and Ap3, Ap4 has higher positive Eu anomalies (Fig. 7d), which can be formed from a change in the oxidation state of the hydrothermal fluid and the resulting reduction of Eu^{3+} to Eu^{2+}. The presence of magnetite and arsenopyrite in the hydrothermal veins containing Ap4 suggests that the oxidation state of the hydrothermal fluids at the late REE (–Cu) remobilization stage was more reduced than that of the early REE (–Cu) remobilization stage. The reduced oxygen fugacity for the hydrothermal fluid responsible for the formation of Ap4 is also consistent with the lowest sulfate intensities in its Raman spectrum among those from all the fluorapatite types in the Yinachang deposit (Fig. 5). These results show that the geochemical and textural features of the altered fluorapatite in the Yinachang deposit are controlled by both the sorption processes and the oxidation state of the hydrothermal fluids. In particular, oxidizing fluids appear to be more conducive for the alteration of fluorapatite allowing for the associated REE to be released from this mineral.

Genesis of Yinachang fluorapatite and implications for REE mineralization

Formation of Ap1 was most likely related to a high temperature magmatic-hydrothermal fluid from Paleoproterozoic dolerite intrusions during the Fe (–REE) mineralization stage. This magmatic–hydrothermal fluid was rich in (REE + Y) and had high carbonate and sulfate contents (Fig. 10a). Ap2 formed from a magmatic-hydrothermal fluid related to Cu mineralization, rich in Cl and S, and depleted in REE + Y (Fig. 10b). Ap3 with high REE contents, and containing REE-rich mineral inclusions, formed after the alteration of REE-rich Ap1 with a high oxidation state, which led to subsequent enrichment in REE in the Neoproterozoic magmatic-hydrothermal fluid (Fig. 10c). Ap4, with the most positive Eu anomalies and the highest Eu contents, was related to a late reduced hydrothermal fluid (Fig. 10d). In conclusion, this study represents a good example of how to use fluorapatite textures and geochemistry to reveal the nature and sources of ore-forming fluids.

Most previous studies of apatite alteration, including Li and Zhou (2015) on fluorapatite from the Yinachang deposit, have emphasized the localized nature of REE remobilization, as evidenced by the formation of REE-rich mineral

inclusions within or beside the apatite grains (Pan et al. 1993; Harlov and Förster, 2003; Bonyadi et al. 2011; Broom-Fendley et al. 2016; Harlov et al. 2016; Hu et al. 2019; Ying et al. 2020). In this study, mass balance calculations for the formation of Ap3, as well as its associated REE-rich inclusions from Ap1, assuming no external contributions of Ca and P, suggests significant leaching of REE during hydrothermal alteration at the Yinachang deposit, which is further supported by the common occurrences of Ap4 and associated REE-rich minerals [monazite–(Ce), bastnaesite–(Ce), and synchysite–(Ce)] in late hydrothermal veins. These results demonstrate that REE remobilization associated with fluorapatite alteration in the Yinachang deposit was not strictly localized in extent, and REE in fluorapatite can also be transported in distance and precipitate as REE-rich minerals associated with other minerals in mineralized veins, which has important implications for upgrading of sub-economic REE mineralization in apatite-rich rocks. Specifically, REE remobilization associated with the hydrothermal alteration of apatite-rich rocks such as those in marine phosphorites, IOCG deposits, and carbonatite deposits (Li et al. 2015; Chakhmouradian et al. 2017; Krneta et al. 2017; Cherry et al. 2018; Algabri et al. 2020), are potentially promoting the mineralization of REE in fluorapatite.

Supplementary Information The online version contains supplementary material available at https://doi.org/10.1007/s00410-021-01849-7.

Acknowledgements This study was funded by the Guang Dong Major Project of Basic and Applied Basic Research (2019B030302013), the National Natural Science Foundation of China (42173065 and 41725009), and the Strategic Priority Research Program of the Chinese Academy of Sciences (XDB42020404).

References

Algabri M, She ZB, Jiao LX, Papineau D, Wang GQ, Zhang C, Tang DJ, Ouyang G, Zhang YG, Chen GY, Li C (2020) Apatite-glauconi association in the ediacaran doushantuo formation, South China and implications for marine redox conditions. Precambrian Res 347:105842. https://doi.org/10.1016/j.precamres.2020.105842

Andersson SS, Wagner T, Jonsson E, Fusswinkel T, Whitehouse MJ (2019) Apatite as a tracer of the source, chemistry and evolution of ore-forming fluids: the case of the olserum-djupedal REE-phosphate mineralisation, SE Sweden. Geochim Cosmochim Acta 255:163–187. https://doi.org/10.1016/j.gca.2019.04.014

Awonusi A, Morris MD, Tecklenburg MMJ (2007) Carbonate assignment and calibration in the Raman spectrum of apatite. Calcif Tissue Int 81:46–52. https://doi.org/10.1007/s00223-007-9034-0

Battsengel A, Batnasan A, Narankhuu A, Haga K, Watanabe Y, Shibayama A (2018) Recovery of light and heavy rare earth elements from apatite ore using sulphuric acid leaching, solvent extraction and precipitation. Hydrometallurgy 179:100–109. https://doi.org/10.1016/j.hydromet.2018.05.024

Bau M (1991) Rare-earth element mobility during hydrothermal and metamorphic fluid-rock interaction and the significance of the oxidation state of europium. Chem Geol 93:219–230. https://doi.org/10.1016/0009-2541(91)90115-8

Bernard PC, Van Grieken RE, Eisma D (1986) Classification of estuarine particles using automated electron microprobe analysis and multivariate techniques. Environ Sci Technol 20:467–473. https://doi.org/10.1021/es00147a005

Bonyadi Z, Davidson GJ, Mehrabi B, Meffre S, Ghazban F (2011) Significance of apatite REE depletion and monazite inclusions in the brecciated Se–Chahun iron oxide–apatite deposit, Bafq district, Iran: insights from paragenesis and geochemistry. Chem Geol 281:253–269. https://doi.org/10.1016/j.chemgeo.2010.12.013

Bromiley GD (2021) Do concentrations of Mn, Eu and Ce in apatite reliably record oxygen fugacity in magmas? Lithos 384–385:105900. https://doi.org/10.1016/j.lithos.2020.105900

Broom-Fendley S, Styles MT, Appleton JD, Gunn G, Wall F (2016) Evidence for dissolution-reprecipitation of apatite and preferential LREE mobility in carbonatite-derived late-stage hydrothermal processes. Am Miner 101:596. https://doi.org/10.2138/am-2016-5502CCBY

Chakhmouradian AR, Reguir EP, Zaitsev AN, Couëslan C, Xu C, Kynický J, Mumin AH, Yang P (2017) Apatite in carbonatitic rocks: compositional variation, zoning, element partitioning and petrogenetic significance. Lithos 274–275:188–213. https://doi.org/10.1016/j.lithos.2016.12.037

Cherry AR, Kamenetsky VS, McPhie J, Thompson JM, Ehrig K, Meffre S, Kamenetsky MB, Krneta S (2018) Tectonothermal events in the olympic IOCG province constrained by apatite and REE-phosphate geochronology. Aust J Earth Sci 65:643–659. https://doi.org/10.1080/08120099.2018.1465473

Chew DM, Spikings RA (2015) Geochronology and thermochronology using apatite: time and temperature, lower crust to surface. Elements 11:189–194. https://doi.org/10.2113/gselements.11.3.189

Engi M (2017) Petrochronology based on ree-minerals: monazite, allanite, xenotime, apatite. Rev Mineral Geochem 83:365–418. https://doi.org/10.2138/rmg.2017.83.12

Fleet ME, Pan YM (1995) Crystal chemistry of rare earth elements in fluorapatite and some calc-silicates. Eur J Mineral 7:591–605. https://doi.org/10.1127/ejm/7/3/0591

Harlov DE (2015) Apatite: a fingerprint for metasomatic processes. Elements 11:171–176. https://doi.org/10.2113/gselements.11.3.171

Harlov DE, Förster H Jr (2003) Fluid-induced nucleation of (Y+REE)-phosphate minerals within apatite: nature and experiment. Part II. Fluorapatite. Am Miner 88:1209–1229. https://doi.org/10.2138/am-2003-8-905

Harlov DE, Wirth R, Förster HJ (2005) An experimental study of dissolution–reprecipitation in fluorapatite: fluid infiltration and the formation of monazite. Contrib Mineral Petrol 150:268–286. https://doi.org/10.1007/s00410-005-0017-8

Harlov DE, Meighan CJ, Kerr ID, Samson IM (2016) Mineralogy, chemistry, and fluid-aided evolution of the pea ridge fe oxide-(Y + REE) deposit, Southeast Missouri, USA*. Econ Geol 111:1963–1984. https://doi.org/10.2113/econgeo.111.8.1963

Haxel G (2002). Rare earth elements: critical resources for high technology, United States Geological Survey Fact Sheet

Hoshino M, Sanematsu K, Watanabe Y (2016) REE mineralogy and resources. Handb Phys Chem Rare Earths Elsevier 49:129–291

Hu L, Li YK, Zj Wu, Bai Y, Aj W (2019) Two metasomatic events recorded in apatite from the ore-hosting dolomite marble and implications for genesis of the giant Bayan Obo REE deposit, Inner Mongolia, Northern China. J Asian Earth Sci 172:56–65. https://doi.org/10.1016/j.jseaes.2018.08.022

Hughes JM, Rakovan JF (2015) Structurally robust, chemically diverse: apatite and apatite supergroup minerals. Elements 11:165–170. https://doi.org/10.2113/gselements.11.3.165

Klinkhammer GP, Elderfield H, Edmond JM, Mitra A (1994) Geochemical implications of rare earth element patterns in hydrothermal fluids from mid-ocean ridges. Geochim Cosmochim Acta 58:5105–5113. https://doi.org/10.1016/0016-7037(94)90297-6

Krneta S, Cook NJ, Ciobanu CL, Ehrig K, Kontonikas-Charos A (2017) The wirrda well and acropolis prospects, gawler craton, south Australia: insights into evolving fluid conditions through apatite chemistry. J Geochem Explor 181:276–291. https://doi.org/10.1016/j.gexplo.2017.08.004

Li XC, Zhou MF (2015) Multiple stages of hydrothermal REE remobilization recorded in fluorapatite in the paleoproterozoic Yinachang Fe–Cu–(REE) deposit, Southwest China. Geochim Cosmochim Acta 166:53–73. https://doi.org/10.1016/j.gca.2015.06.008

Li XH, Li ZX, Sinclair JA, Li WX, Carter G (2006) Revisiting the "Yanbian Terrane": implications for neoproterozoic tectonic evolution of the western Yangtze Block, South China. Precambrian Res 151:14–30. https://doi.org/10.1016/j.precamres.2006.07.009

Li XC, Zhao XF, Zhou MF, Chen WT, Chu ZY (2015) Fluid inclusion and isotopic constraints on the origin of the paleoproterozoic yinachang Fe-Cu-(REE) deposit, southwest China. Econ Geol 110:1339–1369. https://doi.org/10.2113/econgeo.110.5.1339

Mao M, Rukhlov AS, Rowins SM, Spence J, Coogan LA (2016) Apatite trace element compositions: a robust new tool for mineral exploration*. Econ Geol 111:1187–1222. https://doi.org/10.2113/econgeo.111.5.1187

McDowell FW, McIntosh WC, Farley KA (2005) A precise 40Ar–39Ar reference age for the Durango apatite (U–Th)/He and fission-track dating standard. Chem Geol 214:249–263. https://doi.org/10.1016/j.chemgeo.2004.10.002

Ohmoto H, Rye RO (1979) Isotopes of sulfur and carbon. In: Barnes HL (ed) Geochemistry of hydrothermal ore deposits, 2nd edn. Wiley-Interscience, New York

Pan YM, Fleet ME (2002) Compositions of the apatite-group minerals: substitution mechanisms and controlling factors. Rev Mineral Geochem 48:13–49. https://doi.org/10.2138/rmg.2002.48.2

Pan YM, Fleet ME, Macrae ND (1993) Oriented monazite inclusions in apatite porphyroblasts from the Hemlo gold deposit, Ontario, Canada. Miner Mag 57:697–707. https://doi.org/10.1180/minmag.1993.057.389.14

Putnis A (2009) Mineral replacement reactions. Rev Mineral Geochem 70:87–124. https://doi.org/10.2138/rmg.2009.70.3

Rakovan J, Newville M, Sutton S (2001) Evidence of heterovalent europium in zoned Llallagua apatite using wavelength dispersive XANES. Am Miner 86:697–700. https://doi.org/10.2138/am-2001-5-610

Song WL, Xu C, Smith MP, Chakhmouradian AR, Brenna M, Kynický J, Chen W, Yang YH, Deng M, Tang HY (2018) Genesis of the world's largest rare earth element deposit, Bayan Obo, China: protracted mineralization evolution over ~1 b.y. Geology 46:323–326. https://doi.org/10.1130/g39801.1

Su ZK, Zhao XF, Li XC, Zhou MF, Kennedy AK, Zi JW, Spandler C, Yang YH (2021) Unraveling mineralization and multistage hydrothermal overprinting histories by integrated in situ U-Pb and Sm-Nd isotopes in a paleoproterozoic breccia-hosted iron oxide copper-gold deposit, SW China. Econ Geol. https://doi.org/10.5382/econgeo.4840

Thomson SN, Gehrels GE, Ruiz J, Buchwaldt R (2012) Routine low-damage apatite U-Pb dating using laser ablation–multicollector–ICPMS. G-Cubed. https://doi.org/10.1029/2011GC003928

Ye XT, Zhu WG, Zhong H, He DF, Ren T, Bai ZJ, Fan HP, Hu WJ (2013) Zircon U-Pb and chalcopyrite Re–Os geochronology, REE geochemistry of the Yinachang Fe–Cu–REE deposit in Yunnan Province and its geological significance. Acta Petrol Sin 29:1167–1186 (**in Chinese with English abstract**)

Ying YC, Chen W, Simonetti A, Jiang SY, Zhao KD (2020) Significance of hydrothermal reworking for REE mineralization associated with carbonatite: constraints from in situ trace element and C-Sr isotope study of calcite and apatite from the Miaoya carbonatite complex (China). Geochim Cosmochim Acta 280:340–359. https://doi.org/10.1016/j.gca.2020.04.028

Zeng LP, Zhao XF, Li XC, Hu H, McFarlane C (2016) In situ elemental and isotopic analysis of fluorapatite from the Taocun magnetite-apatite deposit, Eastern China: constraints on fluid metasomatism. Am Mineral 101:2468–2483. https://doi.org/10.2138/am-2016-5743

Zhao XF, Zhou MF, Li JW, Sun M, Gao JF, Sun WH, Yang JH (2010) Late paleoproterozoic to early mesoproterozoic dongchuan group in Yunnan, SW China: implications for tectonic evolution of the yangtze block. Precambrian Res 182:57–69. https://doi.org/10.1016/j.precamres.2010.06.021

Zhao XF, Zhou MF, Li JW, Selby D, Li XH, Qi L (2013) Sulfide Re-Os and Rb-Sr isotope dating of the Kangdian IOCG metallogenic province, southwest China: implications for regional metallogenesis. Econ Geol 108:1489–1498. https://doi.org/10.2113/econgeo.108.6.1489

Zhao XF, Zhou MF, Gao JF, Li XC, Li JW (2015) In situ Sr isotope analysis of apatite by LA-MC-ICPMS: constraints on the evolution of ore fluids of the Yinachang Fe–Cu-REE deposit, Southwest China. Miner Deposita 50:871–884. https://doi.org/10.1007/s00126-015-0578-z

Zhao XF, Zhou MF, Su ZK, Li XC, Chen WT, Li JW (2017) Geology, geochronology, and geochemistry of the dahongshan Fe-Cu-(Au-Ag) deposit, Southwest China: implications for the formation of iron oxide copper-gold deposits in intracratonic rift settings☼. Econ Geol 112:603–628. https://doi.org/10.2113/econgeo.112.3.603

Zhou MF, Yan DP, Kennedy AK, Li YQ, Ding J (2002) SHRIMP U-Pb zircon geochronological and geochemical evidence for neoproterozoic arc-magmatism along the western margin of the yangtze block, South China. Earth Planet Sci Lett 196:51–67. https://doi.org/10.1016/S0012-821X(01)00595-7

Zhou Y, Huang YX, Pan YM, Mi JX (2009) Single-crystal microtubes of a novel apatite-type compound, (Na2.5Bi2.5)(PO4)3(F, OH), with well-faceted hexagonal cross sections. CrystEngComm 11:1863–1867. https://doi.org/10.1039/B900499H

Zhou MF, Zhao XF, Chen WT, Li XC, Wang W, Yan DP, Qiu HN (2014) Proterozoic Fe–Cu metallogeny and supercontinental cycles of the southwestern Yangtze Block, southern China and northern Vietnam. Earth-Sci Rev 139:59–82. https://doi.org/10.1016/j.earscirev.2014.08.013